Autonomous Mapping of Underwater Magnetic Fields Using a Surface Vehicle

JONGDAE JUNG, (Member, IEEE), **JEONGHONG PARK**, (Member, IEEE),
JINWOO CHOI, (Member, IEEE), **AND HYUN-TAEK CHOI**, (Member, IEEE)
Marine Robotics Research Department, Korea Research Institute of Ships and Ocean Engineering, Daejeon 34103, South Korea

Corresponding author: Jongdae Jung (jdjung@kriso.re.kr)

ABSTRACT Geomagnetic field signals have potential for use in underwater navigation and geophysical surveys. To map underwater geomagnetic fields, we propose a method that exploits an autonomous surface vehicle. In our system, a magnetometer is rigidly attached to the vehicle and not towed by a cable, minimizing the system's size and complexity but requiring a dedicated calibration procedure due to magnetic distortion caused by the vehicle. Conventional 2-D methods can be employed for the calibration by assuming the horizontal movement of the magnetometer, and the proposed 3-D approach can correct for horizontal misalignment of the sensor. Our method does not require a supporting crane system to rotate the vehicle, and calibrates and maps simultaneously by exploiting data obtained from field operation. The proposed method has been verified experimentally in inland waters, generating a magnetic field map of the test area that is of much higher resolution than the public magnetic field data.

INDEX TERMS Autonomous surface vehicles (ASVs), magnetic field, sensor calibration, underwater mapping.

I. INTRODUCTION

The Earth's magnetic, or geomagnetic, field is a geophysical signal generated by the geodynamo of the Earth's outer core and plays an important role in protecting the Earth from solar winds. Geomagnetic fields, in combination with appropriate georeferences, can also be useful in several underwater applications, including inertial navigation of underwater vehicles, detection of underwater unexploded ordnance or sunken ships, detection and tracking of pipelines, analysis of the Earth's crustal movement, and exploration of mineral resources [1]–[4]. Several organizations periodically publish geomagnetic field maps online, for example, the National Centers for Environmental Information or the International Association of Geomagnetism and Aeronomy. The provided geomagnetic field maps, such as the World Magnetic Model (WMM) [5] and International Geomagnetic Reference Field (IGRF) [6], are generated by aggregating heterogeneous magnetic observations and fitting them to a physical model of the Earth's magnetic field. Although these models support horizontal and vertical continuation, actual field data resolutions are low and it takes a long time to update

the models. Even the commercial High Definition Geomagnetic Model (HDGM) [7] requires one year to update and has a field resolution of several kilometers at crust level. Therefore, developing a technology to construct a high-resolution geomagnetic field map on demand is highly desirable, while the obtained field data will still contribute to the refinement of existing models.

Ground and airborne measurements are commonly used for observing the Earth's magnetic field in terrestrial regions. In marine environments, marine vehicles (ships, underwater gliders, etc.) are often used along with satellite measurements [8]–[10], where marine vehicles are closer to the crust and obtains data with much shorter wavelengths than the satellites. In ship-based observations, the magnetometer is usually towed by cables to reduce the sensor interferences from the thruster or the vehicle itself. However, this arrangement requires additional analysis of the cable's behavior and accurate positioning of the towed sensor, thus resulting in a highly complex overall system. Towing cables also limt the flexibility of the ship's course. In this paper, we have installed a magnetometer rigidly below the main body of our vehicle.
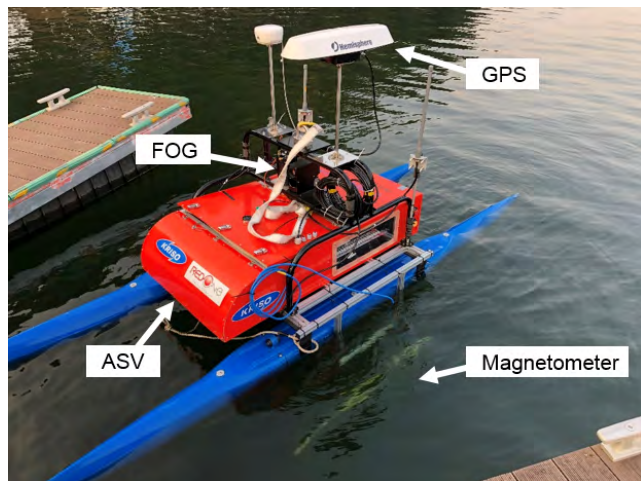
TABLE 1. ASV specifications.

Designation	Value
Length [m]	3.65
Breadth [m]	1.2
Platform weight [kg]	210
Payload [kg]	125
Speed [knots]	up to 2
Propulsion	two electric thrusters (80 lb each)
Power	two LiPo batteries
	control system (24V/30Ah)
	thruster (24V/60Ah)
Motion sensors	GPS-compass (Hemisphere)
	DVL (Teledyne-RDI)
	FOG (Advanced Navigation)

In this way, we simplify the overall mapping system and operate efficiently, with increased flexibility in path generation. However, overcoming the sensor interference caused by thrusters and other electronic vehicle components requires a method to compensate the magnetometer distortions. Conventional 2D calibration methods [11], [12] can be used for this purpose if the vehicle and sensor move on the horizontal plane. However, this assumptions can be broken when a sensor is misaligned or vehicle's buoyancy is unbalanced. Therefore, we develop a 3D calibration method that employs an additional orientation sensor. The calibrated magnetic field data are further processed to build georeferenced field maps.

In the remainder of this paper, the mapping system is explained in section II. Details of 2D and 3D magnetometer calibration is described in section III, followed by our proposed field mapping approach in section IV. A field experiment and its result are presented in section V. Finally, conclusions are outlined in section VI.

II. SYSTEM OVERVIEW
A. AUTONOMOUS SURFACE VEHICLE
Autonomous surface vehicle (ASV) systems have been developed to support the unmanned operations such as environment monitoring and data gathering. One such vehicle developed at the KRISO is depicted in Fig. 1. It was designed for easy handling and durability in field environments. Table 1 describes the primary specifications of this ASV. The hardware system of the developed vehicle comprises the following subsystem components:

1) POWER AND PROPULSION MODULE
The vehicle has a catamaran-hull form with two electrical outboard thrusters as the primary propulsion system. The ASV is steered using differential thrust in a nominal operation. The propulsion system is electrically powered by batteries; its operating duration is approximately four hours, depending on operating conditions. Its nominal cruise speed

is approximately 1.5 knots on inland waters. For unexpected situations during field tests, two emergency switches and a remote emergency stop system were installed to physically disconnect the power to the two thrusters.

2) NAVIGATION AND CONTROL MODULE
A global positioning system (GPS) compass and a fiber optic gyroscope (FOG) are used as navigation sensors for estimating the position and orientation of the vehicle in real time. The GPS update rate was configured as 10 Hz, slower than the FOG (100 Hz) sensor. Two embedded computers are equipped on the vehicle: the primary computer handles navigation, control, and system management. The secondary computer processes data obtained from the underwater sensors (i.e., a magnetometer, doppler velocity log (DVL), and two-hydrophone array). These two computers are connected via a TCP/IP communication link. A wireless local area network (WLAN) communication device and a radio frequency (RF) modem are used to reciprocally communicate the ASV's status and commands with the station. In addition, all devices and sensors are controlled by an interface board that we developed.

B. NAVIGATION, GUIDANCE AND CONTROL
For navigation in the horizontal plane, the ASV's motion is typically simplified as a three degree-of-freedom (DOF) kinematic vehicle model. Waypoint tracking guidance is an essential maneuvering capability for autonomous operations [13]. Waypoints are predefined according to the survey area. In waypoint tracking guidance, line-of-sight (LOS) and cross-track guidance approaches are employed to minimize the error corresponding to the straight path generated between waypoints, as shown in Fig. 2. These errors can be expressed as

- LOS guidance:

$$\psi_d = \tan^{-1}\left(\frac{y_t - y_c}{x_t - x_c}\right) \qquad (1)$$
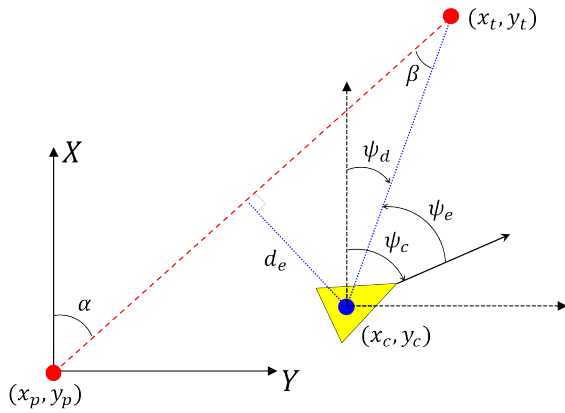
$$\psi_e = \psi_d - \psi_c \qquad (2)$$

FIGURE 2. Waypoint tracking guidance.

- Cross-track guidance:

$$\alpha = \tan^{-1}\left(\frac{y_t - y_p}{x_t - x_p}\right) \tag{3}$$

$$\beta = \alpha - \psi_d \tag{4}$$

$$d_e = \sin\beta\sqrt{(x_t - x_c)^2 + (y_t - y_c)^2} \tag{5}$$

where (x_p, y_p) and (x_t, y_t) are the preceding and the target waypoints in (x, y) coordinates, respectively; (x_c, y_c) is the current position of the vehicle; ψ_c is the heading angle; and ψ_e and d_e denote the LOS and cross-track errors.

A three-DOF motion model is employed in the ASV's control system design and a conventional proportional-derivative controller is applied to determine the required force vector for waypoint tracking control of the ASV in the horizontal plane.

C. PAYLOADS

Payloads include a GPS receiver, magnetometer, and gyroscope. Magnetometers can be classified as scalar or vector sensors according to whether they measure the total field strength F or field vector. In this study, a fluxgate magnetometer is used, which gives three-component field values $\boldsymbol{m} = [m_x, m_y, m_z]^T$ observed in a vehicle body-fixed frame (BFF). The attitude information must be provided to express $\boldsymbol{m}$ in a reference frame. To this end, an FOG is installed in our vehicle. The FOG measurements are also used in the 3D magnetometer calibration described in the next section.

III. MAGNETOMETER CALIBRATION

Since magnetometers suffer from distortions caused by the surrounding electromagnetic field, proper calibration is required to obtain desired magnetic field values. In this study, the magnetometer is rigidly attached below the vehicle, but the sensor is still affected by the vehicle's control box and thrusters. Typical procedure for magnetometer calibration is composed of the following two steps:

1) Sufficient free rotation of the sensor around three rotation axes, creating an ellipsoid of field measurements.
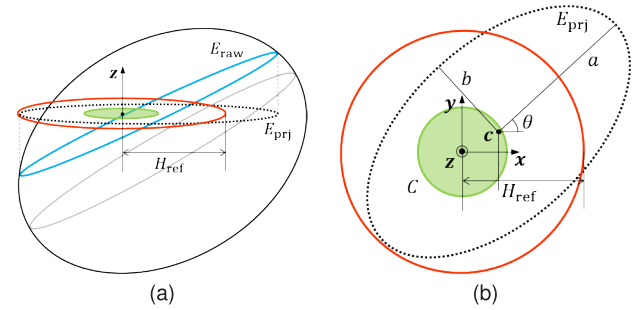2) Conversion of the ellipsoid into a sphere centered at the origin, which removes distortions caused by hard/soft

FIGURE 3. 2D calibration method: (a) ellipses of raw (E_{raw}) and projected (E_{prj}) data, (b) shifting and rescaling E_{prj} by the horizontal component H_{ref} of the reference magnetic field.

iron effects, sensor misalignment, and scale factor error.

However, for huge, heavy systems like our vehicle, rotating the vehicle and sensor around is difficult even for a single rotation axis, requiring special equipment such as cranes. In this work, we eliminate the motion required in Step 1 by exploiting sensor data obtained from field operation, not from a seperate calibration procedure. Therefore, our method simultaneously solves calibration and mapping problems.

A. 2D CALIBRATION

Conventional 2D magnetometer calibration [12] accurately estimates headings if the sensor moves on a horizontal plane. This method can also be applied to surface vehicles that move in a way that generates angular displacement dominant in the yaw direction. Ideally, if the vehicle's yaw displacement is sufficient, the resulting magnetometer measurements produce a horizontal circle on a sphere. However, due to magnetometer distortions, actual sensor values make an ellipse on an ellipsoid, as shown in Fig. 3. The raw ellipse E_{raw} is projected onto a horizontal plane to obtain a new ellipse E_{prj}, which is converted to a unit circle C, maintaining orientation angle θ. Thus, we can remove magnetometer distortions and use the calibrated output for heading estimation. The detailed calculation procedure is as follows:

$$\boldsymbol{m}_h = (\boldsymbol{n}_h^T \boldsymbol{m})\boldsymbol{n}_h \tag{6}$$

$$\boldsymbol{m}_\perp = -\text{sgn}(\boldsymbol{m}_h^T \boldsymbol{m}_h)|\boldsymbol{m}_h|\tan\phi \begin{bmatrix} 0 \\ 0 \\ 1 \end{bmatrix} \tag{7}$$

$$\boldsymbol{m}_\parallel = \boldsymbol{m} - \boldsymbol{m}_\perp \tag{8}$$

$$\boldsymbol{m}_{2D} = R_z(\theta)^T \text{diag}\left(\frac{1}{a}, \frac{1}{b}, 1\right) R_z(\theta) \cdot (\boldsymbol{m}_\parallel - \boldsymbol{c}) \tag{9}$$

where $\boldsymbol{n}$ is the normal vector of E_{raw}; $\boldsymbol{n}_h$ is the horizontal direction vector of $\boldsymbol{n}$; $\boldsymbol{m}_h$ is the projection of $\boldsymbol{m}$ along the direction of $\boldsymbol{n}_h$; ϕ is the angle between the $\boldsymbol{n}$ and z-axes; $\boldsymbol{m}_\perp$ and $\boldsymbol{m}_\parallel$ are the vertical and parallel direction vector of $\boldsymbol{m}$, respectively; θ, a, and b are the orientation angle, major and minor axis lengths, and center point coordinates of E_{prj}, respectively. Since all the field values are corrected onto a unit circle through (9) (i.e. $||[m_{2D,x}, m_{2D,y}]^T|| \simeq 1$), $\boldsymbol{m}_{2D}$
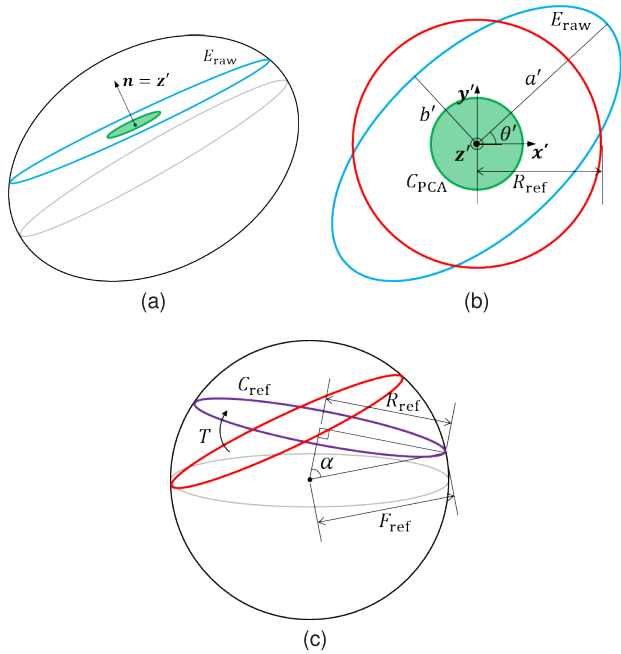
FIGURE 4. 3D calibration method: (a) an ellipse of raw (E_{raw}) data and its normal vector n, (b) rescaling E_{raw} by PCA and the radius R_{ref} of the reference magnetic field, (c) final calibration by finding the best-fit transformation into a referent magnetic field.

FIGURE 5. The Lake Jangseong test site and five ASV trajectories for data gathering.

must be multiplied by a proper scale factor to obtain the actual geomagnetic field. In this work, the values provided by the WMM are used as a reference magnetic field vector. Because the wavelength of the WMM grid is several scores of kilometers, we can choose any point in the mapping area as a reference point. The scaling is calculated as follows:

$$\hat{m}_{2D} = \begin{bmatrix} H_{ref} m_{2D,x} \\ H_{ref} m_{2D,y} \\ m_{2D,z} \end{bmatrix} \quad (10)$$

where H_{ref} is the horizontal field strength of the reference magnetic field.

B. 3D CALIBRATION

The preceding 2D calibration method may fail if the horizontal movement assumption does not hold, which may happen in real applications for two reasons: 1) it is hard to perfectly balance a vehicle on the water's surface due to the weight of payloads and thrusters and 2) sensors can be misaligned during installation. Magnetometer readings are quite sensitive to even small roll and pitch displacements, leading to biased measurements that are undesirable for mapping. Therefore, we propose a calibration method that handles horizontal sensor misalignment by employing an additional gyroscope sensor. The overall procedure for the proposed method is shown in Fig. 4. First, a reference magnetic field vector m_{ref}^{IRF} represented in an inertial reference frame (IRF) is converted into the virtual observations m_{ref}^{BFF}, the expected reference field measurements represented in a BFF. Orientation of the vehicle body from a gyroscope is used for this purpose,
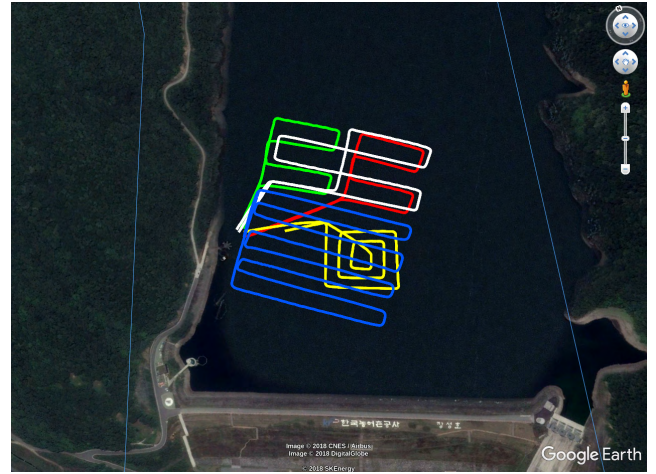
described as follows:

$$m_{ref}^{BFF} = R_{IRF}^{BFF} m_{ref}^{IRF} \quad (11)$$

where R is a directional cosine matrix describing the rotation between the BFF and IRF. Then, we apply principal component analysis (PCA) to the raw measurement and find the best-fit plane P. After that, E_{raw} is converted to a unit circle C_{PCA} on the P, as in (9):

$$m_{PCA} = R_z(\theta')^T \text{diag}\left(\frac{1}{a'}, \frac{1}{b'}, 1\right) R_z(\theta') \cdot (m') \quad (12)$$

where θ', a', and b' are the orientation angle and major and minor axis length of the PCA-transformed ellipse, respectively. Then, the measurements are re-scaled by R_{ref}, a radius of reference measurements, as in 10:

$$\hat{m}_{PCA} = \begin{bmatrix} R_{ref} m_{PCA,x} \\ R_{ref} m_{PCA,y} \\ m_{PCA,z} \end{bmatrix} \quad (13)$$

wehre R_{ref} is calculated as follows:

$$R_{ref} = F_{ref} \sin \alpha \quad (14)$$

$$\alpha = \Sigma_{i=1}^{N} \cos^{-1}\left(\frac{\{m_{ref}^{BFF}\}_i}{||\{m_{ref}^{BFF}\}_i||} \cdot \frac{n_{ref}}{||n_{ref}||}\right) \quad (15)$$

where F_{ref} is the total field strength of the reference magnetic field vector, $\{m_{ref}^{BFF}\}_i$ is the i-th reference magnetic field observation, n is the normal vector of the reference circle C_{ref}, and N is the number of observations. A best-fit transformation T between m_{ref} and m_{PCA} is then obtained as follows:

$$T = \begin{bmatrix} R & t \\ 0 & 1 \end{bmatrix}$$
$$= Kabsch(\hat{m}_{PCA}, m_{ref}^{BFF}) \quad (16)$$

where R is a rotation matrix and t is a translation vector. For the 3D transformation, we used the Kabsch algorithm [14],
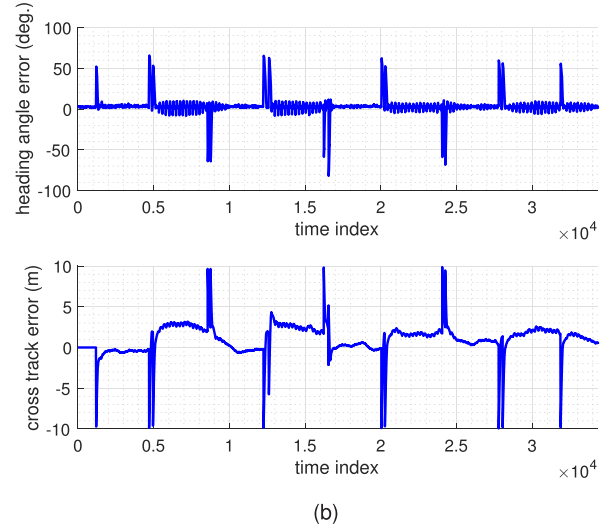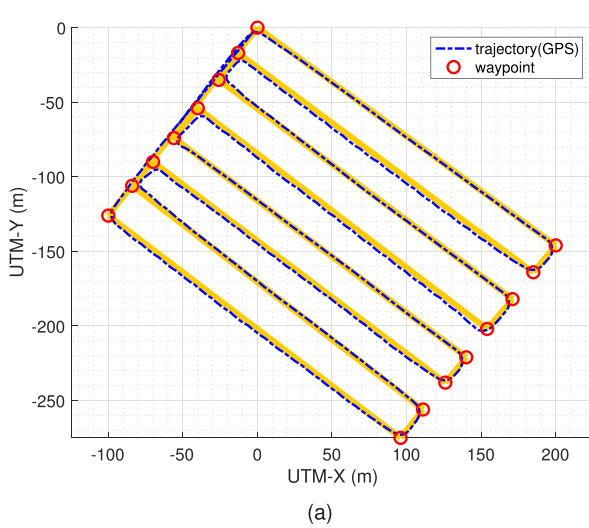
FIGURE 6. Field test results for waypoint tracking: (a) waypoints and actual trajectory of the ASV, (b) heading angle and cross-track errors.

a least root mean square method. Finally, 3D calibration is applied by following step:

$$\boldsymbol{m}_{3D} = R \cdot \hat{\boldsymbol{m}}_{PCA} + \boldsymbol{t}. \tag{17}$$

IV. MAGNETIC FIELD MAPPING

To be able to use the calibrated field measurements as a map in real applications such as surveys or navigations, all the field values must be represented in a predefined reference coordinate system. Another practical problem is that the resulting map is very sparse, since field data are aquired only along the vehicle's path, and further interpolation is needed to make the map dense.

A. MAP COORDINATE SYSTEMS

In this paper, we conveniently choose a universal transverse Mercator (UTM) coordinate system as an IRF, but any other global coordinate systems can be selected depending on the applications. Conversion of the geomagnetic field values from the BFF to UTM coordinate system can be done as follows:

$$\boldsymbol{m}^{UTM} = \begin{bmatrix} m_x^{UTM} \\ m_y^{UTM} \\ m_z^{UTM} \end{bmatrix}$$
$$= (R_{UTM}^{BFF})^{-1} \cdot (\hat{\boldsymbol{m}}_{2D} \text{ or } \boldsymbol{m}_{3D}). \tag{18}$$

The three components of $\boldsymbol{m}^{UTM}$ can also be represented by one of the widely used field map expressions: total strength F, declination D, and inclination I. The conversion is calculated as follows:

$$F = ||\boldsymbol{m}^{UTM}|| \tag{19}$$

$$D = \tan^{-1}\left(\frac{m_y^{UTM}}{m_x^{UTM}}\right) \tag{20}$$

$$I = \tan^{-1}\left(\frac{m_z^{UTM}}{\sqrt{m_x^{UTM2} + m_y^{UTM2}}}\right). \tag{21}$$

B. MAP INTERPOLATION

To densify the initial sparse map acquired from sensor data, we employed Gaussian process regression (GPR) [15], one of the nonparametric regression methods. In the GPR, the probability of the functions with two domains is defined as a normal distribution:

$$p(f(\boldsymbol{x}), f(\boldsymbol{x}')) = N(\boldsymbol{\mu}, \Sigma). \tag{22}$$

Here, the mean ($\boldsymbol{\mu}$) and covariance (Σ) of the functions are described as follows:

$$\boldsymbol{\mu} = \begin{bmatrix} \mu(\boldsymbol{x}) \\ \mu(\boldsymbol{x}') \end{bmatrix}, \quad \Sigma = \begin{bmatrix} K(\boldsymbol{x}, \boldsymbol{x}) + \sigma_n^2 I & K(\boldsymbol{x}, \boldsymbol{x}') \\ K(\boldsymbol{x}', \boldsymbol{x}) & K(\boldsymbol{x}', \boldsymbol{x}') \end{bmatrix} \tag{23}$$

where σ_n is Gaussian noise variance in function observations and K is a kernel that can be designed according to the problems. In this work, we apply a relatively simple squared exponential kernel such as

$$K(\boldsymbol{x}, \boldsymbol{x}') = \sigma_f^2 \exp\left(-\frac{||\boldsymbol{x} - \boldsymbol{x}'||^2}{2l^2}\right) + \sigma_n^2 \delta(\boldsymbol{x}, \boldsymbol{x}') \tag{24}$$

where $\delta(\cdot)$ is a Kronecker delta function, σ_f is signal variance, and l is length-scale. Assuming zero mean for the prior (i.e., $\boldsymbol{\mu} = \boldsymbol{0}$), the regression is calculated as follows:

$$\mathbb{E}(f') = K(\boldsymbol{x}', \boldsymbol{x})[K(\boldsymbol{x}, \boldsymbol{x})^{-1} + \sigma_n^2 I]\boldsymbol{y} \tag{25}$$
$$\text{cov}(f') = K(\boldsymbol{x}', \boldsymbol{x}')$$
$$\quad - K(\boldsymbol{x}', \boldsymbol{x})[K(\boldsymbol{x}, \boldsymbol{x}) + \sigma_n^2 I]^{-1} K(\boldsymbol{x}, \boldsymbol{x}') \tag{26}$$

where $\mathbb{E}(f')$ and $\text{cov}(f')$ are the mean and covariance of the target function $f(\boldsymbol{x}')$, respectively, and $\boldsymbol{y}$ is the noisy ovservations of $f(\boldsymbol{x})$.
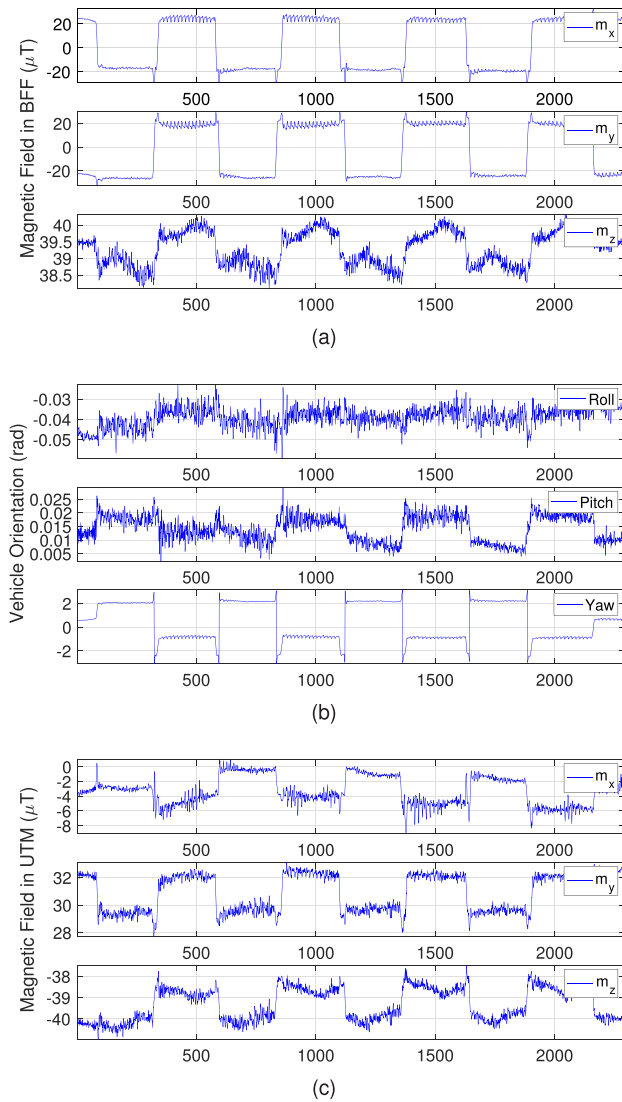
(a)

(b)

(c)

FIGURE 7. Raw sensor readings from (a) magnetometer and (b) FOG; (c) magnetometer readings represented in a global coordinate system (UTM).

TABLE 2. Summary of datasets.

No.	Duration (s)	N	Trajectory (m)
1	1665	1005	993
2	1126	697	880
3	1781	1051	1230
4	1083	663	759
5	3727	2292	2298

V. EXPERIMENTS

We conducted a field test in inland water to verify the proposed mapping system. As previously introduced in Fig. 1, we employed a KRISO-developed ASV in our test. The vehicle's payloads included Hemisphere's V113 GPS, Bartington's Grad-13S magnetometer, and a Spatial FOG from Advanced Navigation. All sensor data were stored with
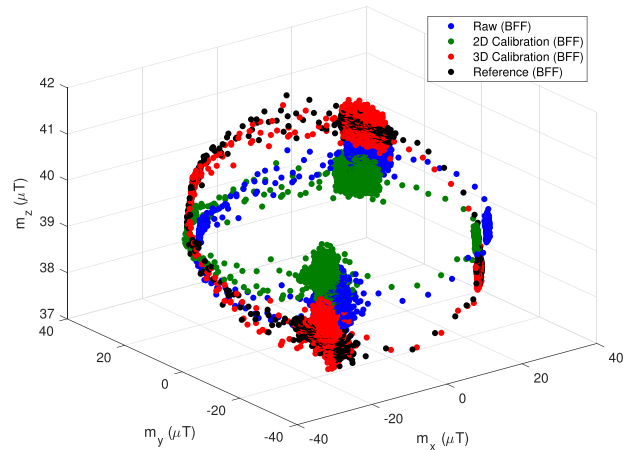

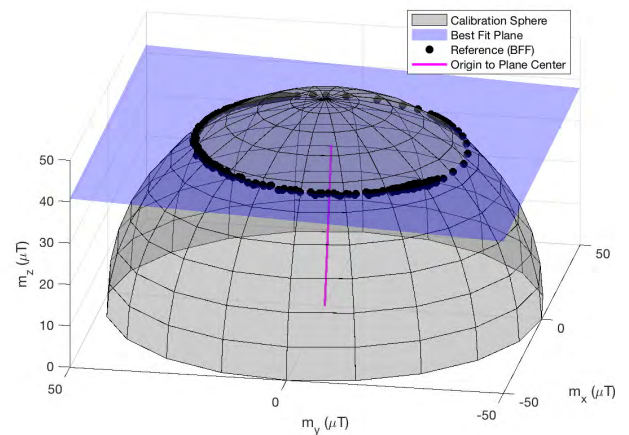**FIGURE 8.** Scatter plot of uncalibrated and calibrated geomagnetic field data, expressed in a body-fixed frame (BFF).

FIGURE 9. A calibration sphere with m_{ref} superimposed on it. The best fit plane and its normal vector *n* represent the horizontal misalignment of the sensor frame.

TABLE 3. Reference magnetic field values (nT).

Component	Value
$m_{\mathrm{ref}}^{\mathrm{UTM}}$	[-4193.5, 30625.7, -39291.1]
H_{ref}	30911.5
F_{ref}	49993.1

timestamps in the vehicle's secondary PC and postprocessed. Fig. 5 shows a satellite image of the test site, Lake Jangseong, located in Korea (35°21′30.2″N, 126°49′17.7″E), and five trajectories that the ASV followed. Table 2 summarizes the gathered datasets. The reference geomagnetic fields used in 10, 11, and 14 are listed in Table 3, as calculated from the WMM corresponding to the experiment's location and date.
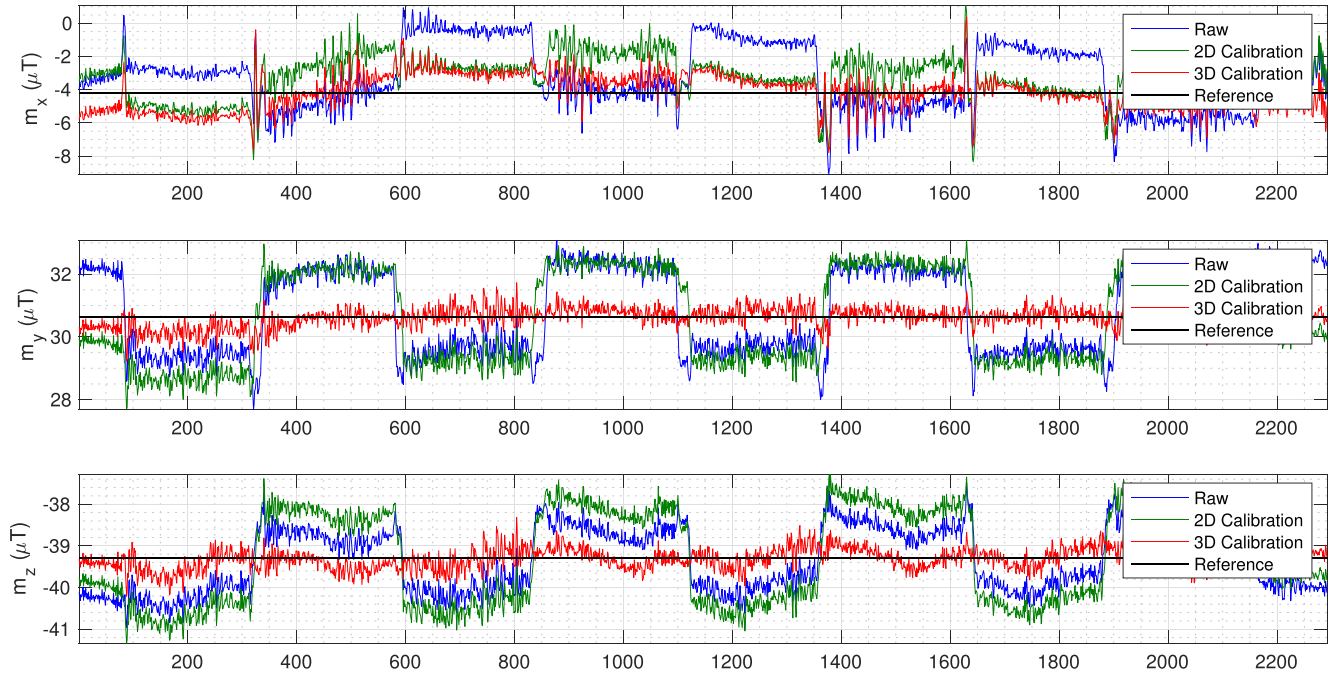
FIGURE 10. Uncalibrated and calibrated geomagnetic field data expressed in a UTM frame. For each plot, the center line represents the reference magnetic field component calculated from the WMM.

TABLE 4. Calibration parameters.

	2D Calibration				3D Calibration					
Data	a (μT)	b (μT)	θ (rad)	c (μT)	a' (μT)	b' (μT)	θ' (rad)	α (rad)	R	t (μT)
1	31.05	30.91	0.000	$\begin{bmatrix} 1.641 \\ -1.636 \end{bmatrix}$	30.94	31.03	1.011	0.658	$\begin{bmatrix} 0.9992 & 0.0401 & 0.0004 \\ -0.0400 & 0.9987 & -0.0327 \\ -0.0017 & 0.0327 & 0.9995 \end{bmatrix}$	$\begin{bmatrix} -2.228 \\ 1.544 \\ 0.420 \end{bmatrix}$
2	30.92	30.94	2.071	$\begin{bmatrix} 1.812 \\ -1.527 \end{bmatrix}$	30.91	30.95	2.324	0.666	$\begin{bmatrix} 0.9999 & -0.0125 & 0.0002 \\ 0.0125 & 0.9994 & -0.0334 \\ 0.0002 & 0.0334 & 0.9994 \end{bmatrix}$	$\begin{bmatrix} -2.488 \\ 1.187 \\ 0.156 \end{bmatrix}$
3	30.94	30.83	1.690	$\begin{bmatrix} 1.948 \\ -1.506 \end{bmatrix}$	30.83	30.94	0.742	0.669	$\begin{bmatrix} 0.9991 & -0.0418 & 0.0011 \\ 0.0418 & 0.9987 & -0.0299 \\ 0.0001 & 0.0299 & 0.9996 \end{bmatrix}$	$\begin{bmatrix} -2.511 \\ 1.137 \\ -0.029 \end{bmatrix}$
4	30.91	30.77	1.786	$\begin{bmatrix} 1.874 \\ -1.472 \end{bmatrix}$	30.80	30.88	0.493	0.670	$\begin{bmatrix} 0.9938 & -0.1111 & 0.0014 \\ 0.1111 & 0.9934 & -0.0300 \\ 0.0019 & 0.0300 & 0.9995 \end{bmatrix}$	$\begin{bmatrix} -2.646 \\ 1.039 \\ -0.113 \end{bmatrix}$
5	30.86	30.95	0.000	$\begin{bmatrix} 1.672 \\ -1.671 \end{bmatrix}$	30.87	30.95	0.763	0.666	$\begin{bmatrix} 0.9997 & 0.0250 & 0.0056 \\ -0.0248 & 0.9990 & -0.0358 \\ -0.0065 & 0.0357 & 0.9993 \end{bmatrix}$	$\begin{bmatrix} -2.270 \\ 1.482 \\ 0.119 \end{bmatrix}$

A. WAYPOINT TRACKING

In the field experimental setup for waypoint tracking control, the ASV moved at a constant speed to minimize the effects of rapid speed variation by the thrusters. The vehicle was controlled to follow the prespecified waypoints and the straight lines between them using the LOS and cross-track guidance laws, as described in (1)–(5). When the desired goal waypoint was changed, the LOS guidance law weight increased and the vehicle's heading angle was converged toward the goal waypoint. Subsequently, the cross-track guidance law weight was increased to quickly follow the straight line.
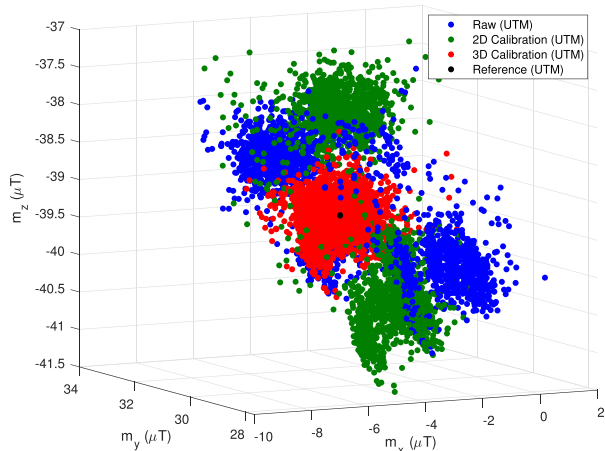
FIGURE 11. Scatter plot of uncalibrated and calibrated geomagnetic field data, expressed in a global coordinate system (UTM).

Fig. 6 shows the results of waypoint tracking on Dataset 5. The vehicle moved 2.3 km over approximately 50 minutes at an average speed of 1.5 knots. The root mean square error (RMSE) of the heading angle error was approximately 13.8°. Variation in the heading angle in the straight-path interval occurred because of the size and shape difference of the sensors mounted on each hull. The RMSE of the cross-track error was approximately 2.08 m, and the instantaneous error rapidly increased at the points where the goal waypoint was changed to be similar to the heading-angle error result.

B. CALIBRATION

The two different calibration methods described in section III were applied to the raw magnetic field data. The resulting calibration parameters are summarized in Table 4. To explore all the details of the calibration procedure, we specifically examined the result from Dataset 5. Fig. 7a and 7b show raw sensor readings from the magnetometer and FOG, respectively. As the magnetometer measures field vectors in a BFF, its measurements are coupled with sensor orientations, especially m_x and m_y. By converting the base coordinate system from BFF to UTM frame using (18), we can remove the frame dependency and obtain field vectors m_{raw}^{UTM} expressed in a global frame, as shown in Fig. 7c. However, m_{raw}^{UTM} still has orientation-dependent biases, caused mainly by soft iron distortion and sensor misalignment.

Fig. 8 shows a scatter plot of the magnetic field data in BFF. Ideally, the reference field data m_{ref} in BFF presents a horizontal circle, since the vehicle moves on the water surface. Here, it produces a slanted circle due to sensor alignment error, which is also verifiable in the FOG data shown in Fig. 7b. The raw data are also slanted, but as an ellipse and not a circle (see parameters in Table 4). The slant angles of m_{raw}^{BFF} and m_{ref}^{BFF} differ as additional hard and soft iron distortions are imposed on m_{raw}^{BFF}. Fig. 9 shows a calibration sphere with m_{ref}^{BFF} superimposed on it. We obtain the best-fit plane using m_{ref}; the resulting plane normal n is used to find
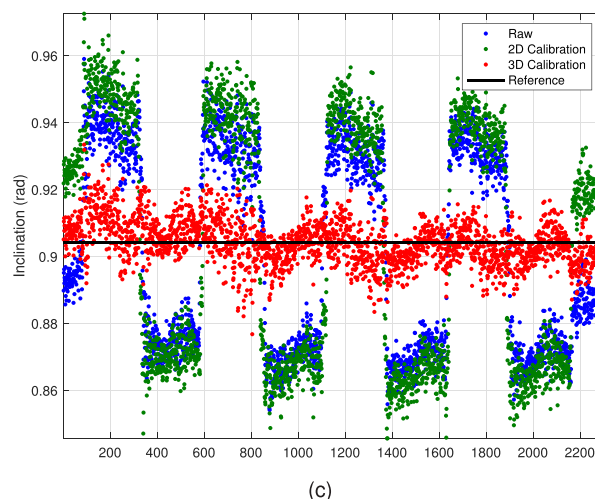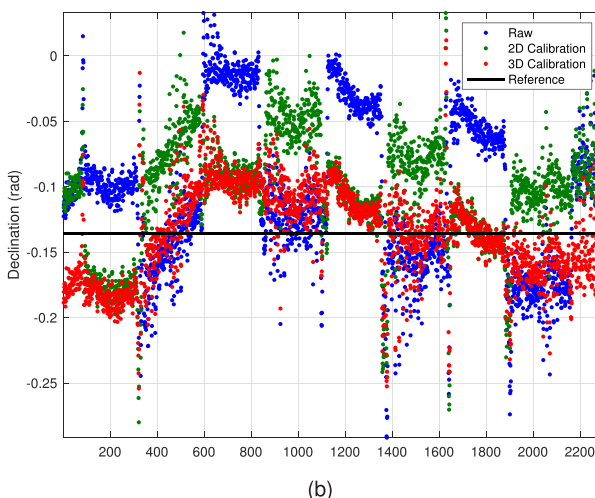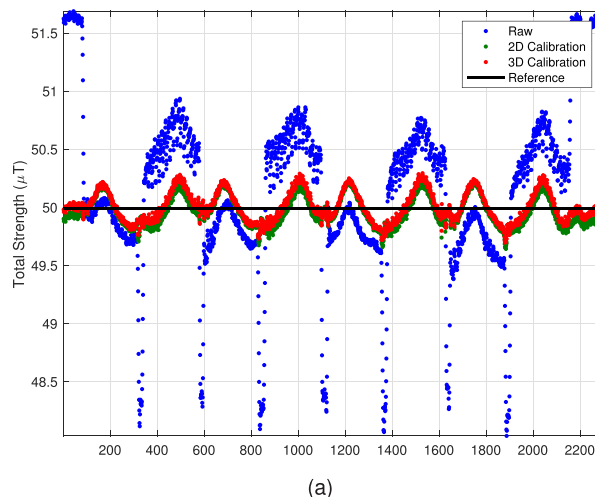

FIGURE 12. Geomagnetic field map components, converted from the results shown in Fig. 10: (a) F, (b) D, and (c) I.

a slant angle α and reference radius R_{ref}, as described in (14) and (15).

Now, 2D calibration projects the raw data onto a horizontal plane, whereas 3D calibration tries to find the best fit to the
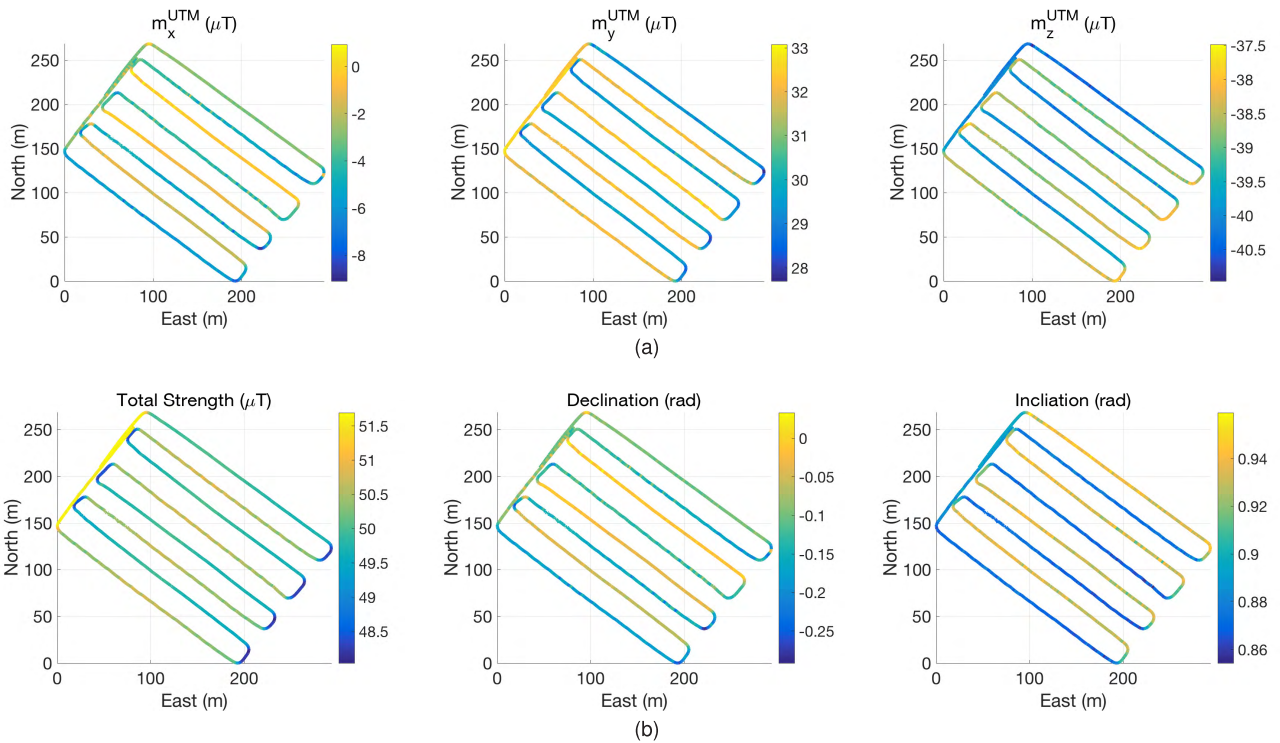
FIGURE 13. Uncalibrated magnetic field data represented in (a) UTM and (b) *F-D-I* components.
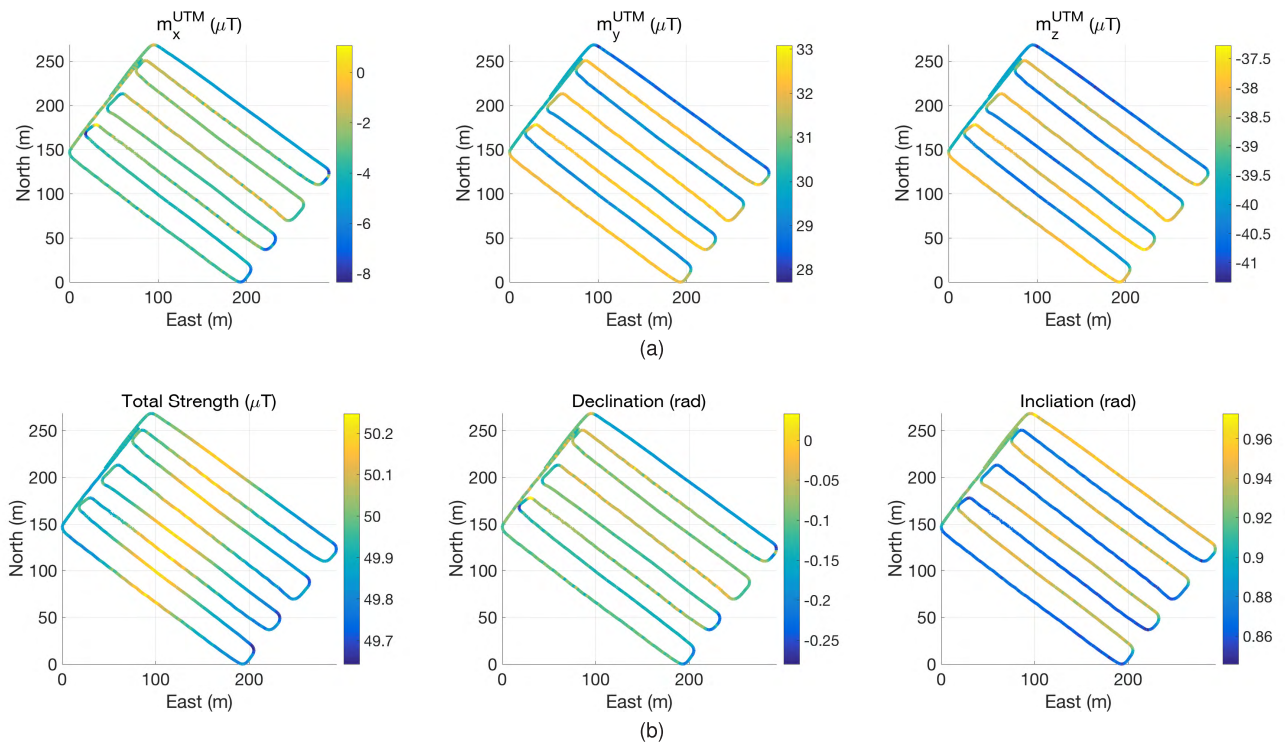

FIGURE 14. 2D calibrated magnetic field data represented in (a) UTM and (b) *F-D-I* components.

reference field using the raw data. Calibration results are shown in Fig. 10, which indicated that the two methods performed differently. Data with 2D calibration still have abrupt changes in all three components and orientation dependency is not resolved. In contrast, 3D calibrated data give continuous sensor readings in all three components and each
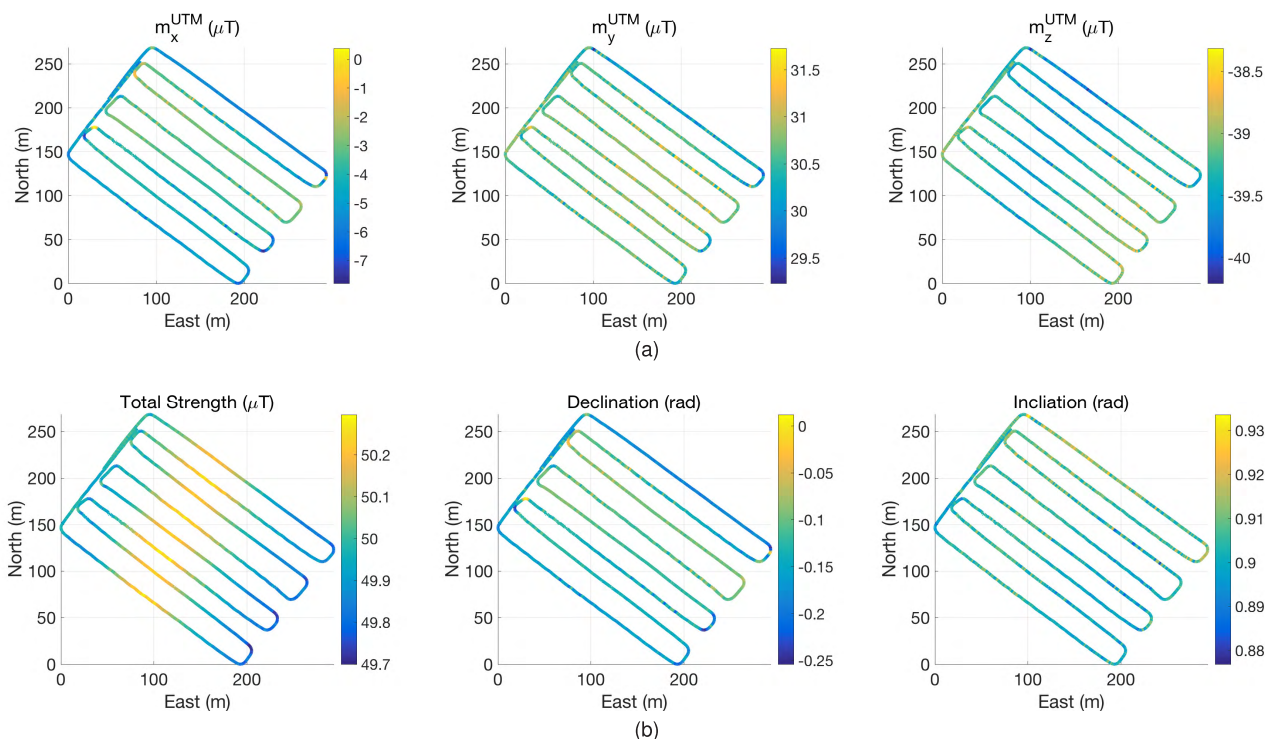
FIGURE 15. 3D calibrated magnetic field data represented in (a) UTM and (b) *F-D-I* components.

component gives values around a reference magnetic field. The calibration result can be more clearly seen in Fig. 11, where we draw a scatter plot again but this time using a UTM frame. Since the test site does not have any strong electromagnetic sources underneath, the desired scatter plot should present a unimodal distribution around the reference field vector. Our 3D calibration shows this distribution, whereas both uncalibrated and 2D calibrated data have multimodal distributions.

C. MAPPING
After the final conversion, as in (19)–(21), we obtained the field map components of *F*, *D*, and *I*, as shown in Fig. 12. Only 3D calibration retrieved the correct field component values. In Figs. 13–15, magnetic field data are mapped in a north-east-down (NED) coordinates with vehicle trajectories. Although uncalibrated and 2D calibrated data suffer from orientation-dependent biases, 3D calibration resolves this problem. The final 3D calibration field map now gives actual field characteristics; *F* has a certain wavelength over the test area and *D* and *I* have only minor variations.

After 3D calibration was applied to all five datasets, we obtained the final map of the magnetic field in the test area, as shown in Fig. 16. Based on this sparse map, GPR was further performed for interpolation; this result is shown in Fig. 17. A relatively high magnetic field value can be observed in the middle of the test area, presumably due to the geophysical properties of the crust underneath. Compared to
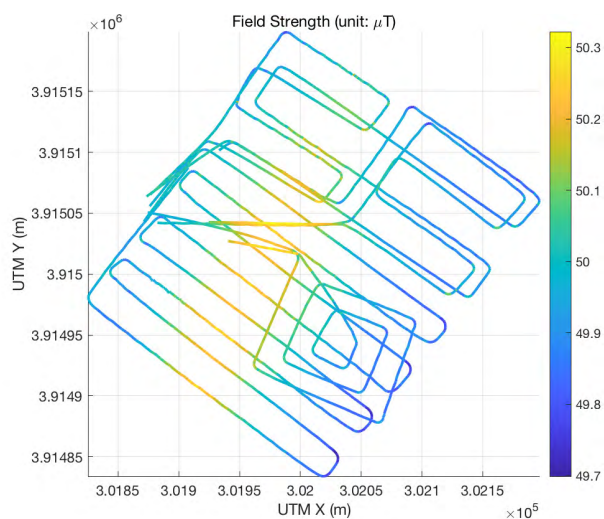

FIGURE 16. Final map of geomagnetic field strength in the test area.

the low resolution of the public geomagnetic field data (e.g., EMAG2-v3 has a 2-arc minute grid [16], which is about 3 km in the test area), the proposed mapping system generated a finer and denser map.

D. DISCUSSION
Conventional 2D calibration method may partially work for determining *F*, as shown in Fig. 14b, because the 2D method projects *x*- and *y*-directional components onto a horizontal
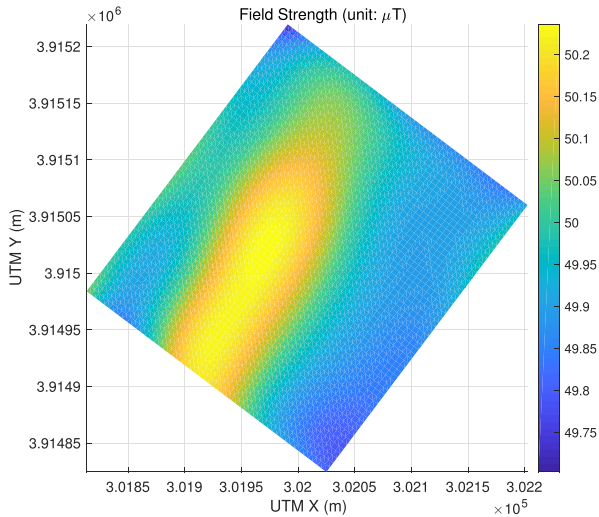
FIGURE 17. Improved mapping (noise reduction and densifying) by GPR.

plane while retaining *z*-directional components. In this way, the field strength magnitude is regularized and becomes independent of the heading angles. However, *D* and *I* are not recovered since m_x, m_y and m_z are not properly calibrated. A full 3D-calibrated magnetic field map is especially important in applications with navigation purposes.

After calibration, magnetic field data still have some noises, as shown in Fig. 12, mainly caused by thrusters, as the noise increases at corner points where the thruster output increases significantly for rotation. Instead of treating this during calibration, we tried to obtain a noise-free map with a GPR. For real-time noise handling, additional approaches such as learning with thruster input voltage are promising.

In this work, we assumed that the mapping target area had no strong external electromagnetic sources, which enabled simultaneous calibration and mapping. If this assumption fails, we can still conveniently use the proposed method separately to obtain calibration parameters and apply them to map the target site.

VI. CONCLUSION
In this paper, we proposed an ASV-based system for mapping underwater magnetic fields. A magnetometer was rigidly attached to the ASV and waypoint tracking was exploited to gather payload data. The proposed approach solves the problem of 3D magnetometer calibration when the typical calibration motion is difficult to achieve. Specifically, the same magnetic field data obtained for mapping were used in the calibration. Compared to the conventional 2D approach, the proposed 3D calibration resolves the orientation-dependent biases caused by soft iron distortion and sensor misalignment. To improve the sparsity of the initial map, we further employed GPR. We conducted experiments in inland water and found that the proposed mapping system shows promise for refining the existing

public database of geomagnetic fields in terms of its possible resolution and update frequency. Future work includes testing the proposed system in ocean environments, downward and upward continuation of the obtained field, and development of a more sophisticated calibration method for real-time compensation.

REFERENCES
[1] S. T. Tuohy, N. M. Patrikalakis, J. J. Leonard, J. G. Bellingham, and C. Chryssostomidis, "AUV navigation using geophysical maps with uncertainty," in *Proc. 8th Int. Symp. Unmanned Untethered Submersible Technol.*, 1993, pp. 265–276.
[2] F. C. Teixeira and A. Pascoal, "Magnetic navigation and tracking of underwater vehicles," in *Proc. 9th IFAC Conf. Control Appl. Marine Syst. (CAMS)*, Osaka, Japan, 2013, pp. 239–244.
[3] Y. H. Pei and H. G. Yeo, "UXO survey using vector magnetic gradiometer on autonomous underwater vehicle," in *Proc. IEEE OCEANS*, Biloxi, MS, USA, Oct. 2009, pp. 1–8.
[4] M. A. Tivey and J. Dyment, "The magnetic signature of hydrothermal systems in slow spreading environments," in *Proc. Diversity Hydrothermal Syst. Slow Spreading Ocean Ridges*, vol. 188, Washington, DC, USA, Aug. 2010 pp. 43–66.
[5] A. Chulliat *et al.*, "The US/UK world magnetic model for 2015-2020," NOAA Nat. Geophys. Data Center, Boulder, CO, USA, Tech. Rep., 2015, doi: 10.7289/V5TB14V7.
[6] E. Thébault *et al.*, "International geomagnetic reference field: The 12th generation," *Earth, Planets Space*, vol. 67, p. 79, Dec. 2015.
[7] S. Maus and C. Manoj, "High-definition geomagnetic models: A new perspective for improved wellbore positioning," in *Proc. IADC/SPE Drilling Conf. Exhibit.*, San Diego, CA, USA, 2012, pp. 1–15.
[8] N. Isezaki, "A new shipboard three-component magnetometer," *Geophysics*, vol. 51, no. 10, pp. 1992–1998, 1986.
[9] J. S. Gee and S. C. Cande, "A surface-towed vector magnetometer," *Geophys. Res. Lett.*, vol. 29, no. 14, pp. 15-1–15-4, 2002.
[10] M. Engels, U. Barckhausen, and J. Gee, "A new towed marine vector magnetometer: Methods and results from a Central Pacific cruise," *Geophys. J. Int.*, vol. 172, no. 1, pp. 115–129, 2008.
[11] J. F. Vasconcelos, G. Elkaim, C. Silvestre, P. Oliveira, and B. Cardeira, "Geometric approach to strapdown magnetometer calibration in sensor frame," *IEEE Trans. Aerosp. Electron. Syst.*, vol. 47, no. 2, pp. 1293–1306, Apr. 2011.
[12] B. Allotta, R. Costanzi, F. Fanelli, N. Monni, and A. Ridolfi, "Single axis FOG aided attitude estimation algorithm for mobile robots," *Mechatronics*, vol. 30, pp. 158–173, Sep. 2015.
[13] K. Y. Pettersen and E. Lefeber, "Way-point tracking control of ships," in *Proc. 40th IEEE Conf. Decis. Control*, Dec. 2001, pp. 940–945.
[14] W. Kabsch, "A solution for the best rotation to relate two sets of vectors," *Acta Crystallographica A*, vol. 32, no. 5, pp. 922–923, 1976.
[15] C. E. Rasmussen and C. K. I. Williams, *Gaussian Processes for Machine Learning*. Cambridge, MA, USA: MIT Press, 2006.
[16] B. Meyer, R. Saltus, and A. Chulliat, "EMAG2 version 3—Update of a two arc-minute global magnetic anomalygrid," in *Proc. EGU Gen. Assembly Conf. Abstr.*, vol. 19, 2017, p. 1.

JONGDAE JUNG received the B.S. degree in civil engineering from Hanyang University, Seoul, South Korea, in 2008, and the M.S. and Ph.D. degrees in civil and environmental engineering from the Korea Advanced Institute of Science and Technology, Daejeon, South Korea, in 2010 and 2015, respectively. He is currently a Senior Researcher with the Korea Research Institute of Ships and Ocean Engineering, Daejeon. His current research interests include marine robotics, underwater perception and navigation, and simultaneous localization and mapping.

JEONGHONG PARK received the B.S. and M.S. degrees in mechatronics engineering from Chungnam National University, Daejeon, South Korea, in 2005 and 2007, respectively, and the Ph.D. degree in mechanical engineering from the Korea Advanced Institute of Science and Technology, Daejeon, in 2016. He is currently a Senior Researcher with the Korea Research Institute of Ships and Ocean Engineering, Daejeon. He has been involved in the areas of ocean robotics, vision-based perception and tracking, and path planning of autonomous ships and marine robots.

HYUN-TAEK CHOI received the B.S., M.S., and Ph.D. degrees in electronic engineering from Hanyang University, Seoul, South Korea, in 1991, 1993, and 2000, respectively. He was an Associate Research Engineer with Korea Telecom from 1993 to 1995. He was with the University of Hawaii, as a Post-Doctoral Researcher, from 2000 to 2003. He is currently a Principal Researcher with the Korea Research Institute of Ships and Ocean Engineering, Daejeon, South Korea. He has been leading several projects related to underwater robotic applications, such as the design of ROVs and AUVs, advanced control and navigation, recognition using optic camera and sonar, and robot intelligence.

• • •

JINWOO CHOI received the B.S., M.S., and Ph.D. degrees in mechanical engineering from the Pohang University of Science and Technology, South Korea, in 2003, 2005, and 2011, respectively. He is currently a Senior Researcher with the Korea Research Institute of Ships and Ocean Engineering, Daejeon, South Korea. His current research interests are mainly concentrated on mapping, localization, SLAM, and acoustic source localization for marine robots.